

Shape-Configurable Mesh for Hernia Repair by Synchronizing Anisotropic Body Motion

Hyunsu Ha, Chan Hee Lee, Kang Suk Lee, Kyubae Lee, Jeongeun Park, Si Yeong Kim, Sewoom Baek, Mi-Lan Kang, Dong Won Lee,* and Hak-Joon Sung*

Continuous progress has been made in elucidating the relationship between material property, device design, and body function to develop surgical meshes. However, an unmet need still exists wherein the surgical mesh can handle the body motion and thereby promote the repair process. Here, the hernia mesh design and the advanced polymer properties are tailored to synchronize with the anisotropic abdominal motion through shape configuration. The thermomechanical property of shape configurable polymer enables molding of mesh shape to fit onto the abdominal structure upon temperature shift, followed by shape fixing with the release of the heat energy. The microstructural design of mesh is produced through finite element modeling to handle the abdominal motion efficiently through the anisotropic longitudinal and transverse directions. The design effects are validated through in vitro, ex vivo, and in vivo mechanical analyses using a self-configurable, body motion responsive (BMR) mesh. The regenerative function of BMR mesh leads to effective repair in a rat hernioplasty model by effectively handling the anisotropic abdomen motion. Subsequently, the device-tissue integration is promoted by promoting healthy collagen synthesis with fibroblast-to-myofibroblast differentiation. This study suggests a potential solution to promote hernia repair by fine-tuning the relationship between material property and mesh design.

of birth that has been diversified in each direction of the body through developmental and adaptative processes. In contrast, the current surgical meshes possess uniform material properties throughout and consistent designs; as a result of which, handling the dynamic anisotropic body motion in parallel and perpendicular directions to gravity is impossible.^[1] Hence, a paradigm shift is required to advance the material property and mesh design with synergistic cooperation incorporating the concept of metamaterials in tailoring mesh's repetitive microstructure,^[2] thermal,^[3] acoustic,^[4] and electromagnetic properties.^[5]


As a target application of the present study, hernia meshes keep internal organs from protruding outward after surgical treatment of muscle or fascia defects in the abdominal wall. Since the mid-20th century, polypropylene (PP), expanded polytetrafluoroethylene (ePTFE), and polyethylene (PE) have been widely used to produce mesh devices.^[6,7] The surgical mesh has evolved to enhance biocompatibility and clinical efficacy by including biological

mesh and degradability in addition to diversifying the design parameters (e.g., structure, pore size, density, weight, filament, etc.).^[8] Despite continuous progress in the surgical method and mesh performance, insufficient regenerative integration between post-surgery tissue and hernia mesh results in complications such as recurrence, fibrosis, and chronic pain.^[9] The

1. Introduction

Each body part generates a unique motion by exerting different direction-dependent properties, thereby limiting the regenerative effect of surgical meshes that are currently in use. This anisotropic motion is inevitable because of the isotropic origin

H. Ha, C. H. Lee, K. Lee, J. Park, S. Y. Kim, H.-J. Sung
Department of Medical Engineering
Yonsei University College of Medicine
50-1 Yonsei-ro, Seodaemun-gu, Seoul 03722, Republic of Korea
E-mail: hj72sung@yuhs.ac

 The ORCID identification number(s) for the author(s) of this article can be found under <https://doi.org/10.1002/smll.202303325>

© 2023 The Authors. Small published by Wiley-VCH GmbH. This is an open access article under the terms of the Creative Commons Attribution-NonCommercial License, which permits use, distribution and reproduction in any medium, provided the original work is properly cited and is not used for commercial purposes.

DOI: 10.1002/smll.202303325

S. Baek, H.-J. Sung
Department of Brain Korea 21 FOUR Project for Medical Science and Medical Engineering
Yonsei University College of Medicine
50-1 Yonsei-ro, Seodaemun-gu, Seoul 03722, Republic of Korea

D. W. Lee
Department of Plastic and Reconstructive Surgery
Institute for Human Tissue Restoration
Yonsei University College of Medicine
Seoul 03722, Republic of Korea
E-mail: xyphoss@yuhs.ac

K. S. Lee, M.-L. Kang, H.-J. Sung
TMD LAB Co. Ltd.
6th floor, 31, Gwangnaruro-ro 8-gil, Seongdong-gu, Seoul 04799, Republic of Korea

previous development of surgical mesh has been focused on the improvement of tensile strength to prevent the structural failure post-implantation.^[10] However, the hernia recurrence is driven predominantly by mismatched mechanical loads at the mesh-tissue interface^[11,12] rather than merely the insufficient tensile strength as seen in the post-surgical complications of existing devices (e.g., poor connective tissue ingrowth, wound contracture, migration, and device damage).^[13] As the abdominal wall is constantly exposed to anisotropic motions with changes in intra-abdominal pressure, it is hypothesized that the motion synchronization between the abdominal wall and the hernia mesh can improve the regenerative effect in this study.

The anisotropic motion synchronization requires a match in the properties of the surgical mesh and the abdominal wall. As a result, this study introduces body motion responsive (BMR) mesh as a testable solution by applying the anisotropic difference between motion-resistant transverse (T) and motion-prone longitudinal (L) directions. Therefore, BMR mesh integrates abdominal characteristics into the mesh property through structural design. As a foundation theory, Maxwell's criterion guides the microstructural design of a single unit to vary each directional rigidity of the whole mesh in the repeated units.^[14] Addition of one string into an isotropic honeycomb unit endows the anisotropic stretch-dominant and bending-dominant properties in the T and L directions, respectively. Spatial rearrangement of single units through further design enables the anisotropic property to match the abdominal wall motion, constituting the design of BMR mesh.

Motion synchronization should accompany the shape-fitting of the hernia mesh into the patient-specific abdominal structure to prevent any disturbances between the abdominal wall and mesh motions. The present study explored unique polymeric properties to endow this key function, thereby enabling efficient handling of anisotropic abdominal motion in cooperation with the BMR mesh design. In semicrystalline polymers, temperature shifts increase the mobility of polymer chains and thereby reduce the stiffness because of the decrystallization process, followed by chain recrystallization upon heat release. These properties provide moldability to the BMR mesh allowing to configure the abdomen shape upon temperature shift, followed by shape fixing as the heat energy is released. However, when the temperature shifts over 50 °C to operate this moldable property, the abdominal tissue gets damaged because of protein denaturation; as a result, the alteration of chain mobility should only occur below 50 °C.

Also, tight holding of polymer chains is required to maintain a basic structure of surgical mesh, even when the molding process occurs around melting temperature (T_m). As a means of tight holding, cross-linking among polymers at inner-chain sites is strategized to design the shape configurable polymer as a form of 96%-polycaprolactone-co-04%-polyglycidyl methacrylate (molar %, PCL-PGMA) so that the cross-linking also reduces T_m together with crystallinity as reported previously.^[15] The mechanical property of PCL-PGMA was enhanced by modifying the polymer structure to have six arms and by further blending with PCL (6-arm-PCL/PCL-PGMA). In this way, the sufficient stiffness of BMR mesh enabled the prevention of internal organs to protrude outward when the abdominal motion generates a peak

pressure. The 6-arm PCL/PCL-PGMA based polymer was 3D printed as pre-examined previously,^[6,16] which provided an efficient and effective tool-box to test diverse designs and patterns of mesh.

It is hypothesized that the anisotropic motion synchronization can drive a phenotypic change in fibroblasts to more mechano-responsive myofibroblasts.^[17] Consequently, the connective tissue of the abdominal wall is regenerated efficiently after hernia surgery by promoting extracellular matrix (ECM) synthesis, including proteoglycan, fibronectin, and hyaluronic acid, thereby maturing the connective tissue.^[18] A mature ECM can prevent hyperplastic scarring reaction by reducing the excessive local stress, thereby justifying the need for motion synchronization. Collagen occupies more than 80% of abdominal wall ECM, and the high ratio of collagen type 1 (Col1) to type 3 (Col3) should be maintained to promote healthy regeneration of the abdominal wall. Because Col1 is strong and thick in contrast to thin, weak, and immature Col3,^[19] a decrease in Col1/3 ratio disorganizes the abdominal ECM composition.^[20,21] As a result, the Col1/3 ratio serves as a prognostic factor post-hernioplasty as previous clinical studies reported.^[20,22] Furthermore, fibroblasts are expected to elongate along with the directional stress that BMR mesh generates upon cyclic motion of the abdomen, thereby producing highly oriented fibers of Col1, acting as another key factor for abdominal wall regeneration.

This study utilized a unique cooperation of mesh design with thermomechanical polymer properties to enable anisotropic motion synchronization between hernia mesh and abdominal wall, thereby promoting the regeneration effect after surgical repair. The anisotropic property of abdominal motion and wall tissue was matched with the mesh design by adding a string into an isotropic honeycomb unit, followed by rearranging the repeated units to complete the mesh structure. The matched property was validated through computational modeling with calculation and experimental examination of rat abdominal motion and the consequent tissue property.

Next, a biocompatible hernia mesh was prepared by synthesizing a PCL-PGMA copolymer in a 6-arm architecture with cross-linking by the acrylic functional groups. This shape memory polymer exhibited the ability to recover its original shape above the melting temperature. Nonetheless, this study was focused on a different aspect of thermal-responsive function by increasing the mobility of polymer chains for shape configuration upon temperature shift and then fixing the shape as the heat energy was released with cooling.^[23,24] The shape with the configurable properties could be adjusted in a user-specified way.^[25] The compositional and structural tuning made the polymer moldable, enabling it to configure in accordance with the abdomen shape upon implantation with sufficient strength. The thermomechanical properties of the polymer were tuned to carry out the shape configuration efficiently with the determination of onset temperature, heating time duration, and Young's modulus in isothermal conditions. Finally, in vitro motion reactor and rat hernioplasty model were assessed to validate that the anisotropic motion synchronization with fine-tuned operation parameters, promoting regenerative fibroblast responses and collagen synthesis leading to clinical translation of hernia repair.

2. Results

2.1. Design Concept and Theory of BMR Mesh

3D printing enables target organ and patient-specific customization of medical devices^[26] and provides a design foundation to support an organ movement with heterogenous mechanical characteristics.^[27] We aimed to generate the versatility to support anisotropic characteristics of abdominal movement by manipulating the design of the device pattern following the emerging paradigm. The stiff T and elastic L motion of the abdomen justified the need for anisotropic stiffness in the mesh design (Figure 1a). As a starting point of the experiment, this justification was validated first by 1.45 times the stiffness in the T modulus over the L direction measured through the *ex vivo* tensile test using rat abdomen tissues post-harvesting (Figure 1b). This result was also confirmed by setting real-time accumulation of two directional fatigues into the polymer films upon attachment onto the rat abdomen depicting daily moving conditions (Figure 1c). As a result of fatigue accumulation, the samples that moved farther failed quicker in response to cyclic strains. Further, the cycle to failure decreased significantly from no motion to the T and further in the L direction films.

Next, the design concept of an anisotropic BMR mesh was developed to synchronize with stiff T and flexible L movements. Maxwell stability criterion^[14] was applied to analyze single-unit designs (Figure S1a, Supporting Information). The stability criterion is given by $M = b - 2j + 3$, where M represents structural stability, b is the number of struts, and j is the number of joints. The basic diamond structure with four joints and four strings exhibited isotropic bending in the direction of force. The addition of string in the perpendicular direction of force promoted resistance to bending, resulting in a stretch-dominant structure. Hence, instead of the diamond structure, this criterion was applied to the honeycomb structure, which also exhibited isotropic bending in the direction of force (Figure S1b, Supporting Information). However, the addition of a single string in the perpendicular direction of bending resulted in T resistance against the dominant L bending, representing the design concept of BMR mesh. The addition of three strings among the six joints made the structure resistant to any force direction. The results from the analyses of single units justified the addition of a string in the perpendicular direction to the bending-prone side so that the anisotropic motion can be handled.

2.2. Computational Modeling of BMR Mesh Design

As a single-unit model of BMR mesh, a string was added in the T direction of each honeycomb unit (isotropic base), following the concept that engineering the microstructure of each of the repeated units can tailor and contribute to the physical properties of the whole structure (Figure 1d).^[27,28] The design of BMR mesh mimicked the role of a bowstring that produces stretch-dominant (T) stiff and bending-dominant (L) elastic properties, thereby operating the anisotropic directional functions to shoot arrows. As a result of the T string addition, the anisotropic distribution of directional modulus was generated in the single unit compared to the isotropic distribution of the entire honeycomb unit. In the further modeling analysis of tensile modulus with a polar chart,

the T direction of the single anisotropic unit was 6.9 times stiffer than the L direction in contrast to no difference in the directional modulus of the single isotropic unit.

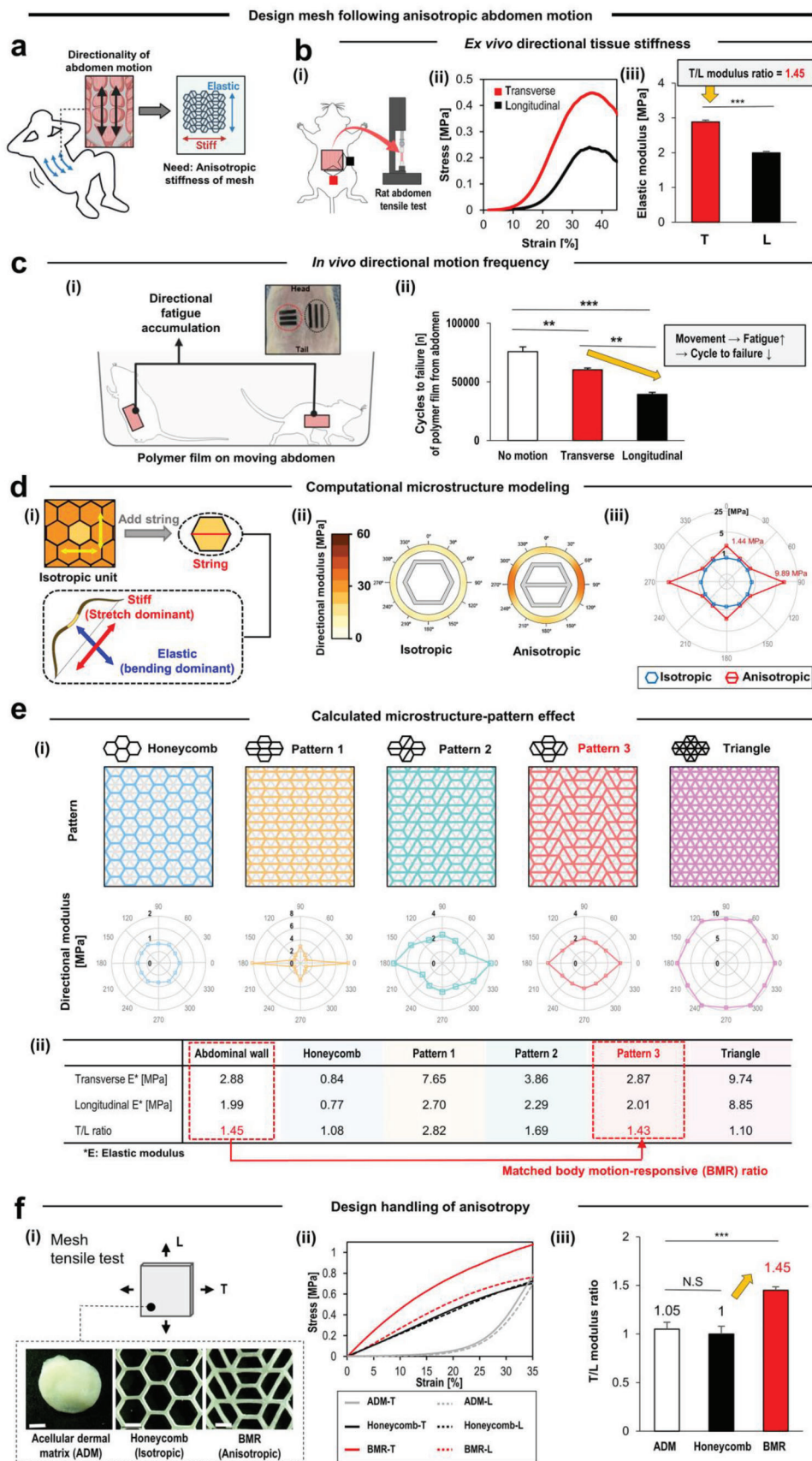
As a basic parameter to rearrange the single units to obtain repeated patterns of mesh design, the connectivity was defined as the number of struts per joint, which served as a determinant factor of structural stiffness (Figure S2, Supporting Information).^[28] The honeycomb mesh presented isotropic bending-dominant characteristics at all points, whereas pattern 1 with uniform string direction became excessively stiff in the T direction compared to the abdominal wall. In contrast, pattern 3 (BMR mesh) reduced the stiffness in the T direction by adjusting the pattern of the string direction, thereby presenting the mixed property of bending and stretching-dominant in alignment with the anisotropic motion of the abdominal wall. Among the repeated pattern candidates from rearrangements of single units, the pattern model to exhibit the 1.45 T/L modulus ratio was determined as suitable, evidenced by the *ex vivo* analysis of abdomen wall tissues (Figure 1e). As candidates, anisotropic repeated patterns (1–3 and Triangle) were generated through 2D spatial rearrangements of the honeycomb microstructure (isotropic base), followed by calculating the distribution of the directional modulus of each pattern. When the T/L modulus ratio was analyzed, the ratio of repeat pattern 3 decreased from 6.9 to 1.43 for the single anisotropic unit which aligned with the ratio of the abdomen wall (1.45), thereby serving as the pattern of BMR mesh.

2.3. Experimental Validation of BMR Mesh Design

PCL/PCL-PGMA was synthesized and subjected to tensile tests to record stress as a function of strain (Figure S3, Supporting Information), resulting in the Young's modulus (MPa) of 78.12 and the Yield strength (MPa) of 7.92. The bilinear isotropic model with elastic parameter as the input was used for computational simulation. The experimental validation of the pattern effect was carried out through tensile tests on an acellular dermal matrix (ADM, commercial control) and on sample meshes with honeycomb (isotropic control) versus anisotropic BMR pattern (Figure 1f). The T and L directions of both honeycomb and BMR meshes exhibited nearly linear relationships between stress and strain, indicating a predictable deformation of up to 35% by controlling the stress. Only the stiff BMR-T required more stress to deform to the same level as the others (BMR-L, honeycomb-T and L) and the levels of stress–strain changes were similar throughout the test range.

Although both directions of ADM exhibited similar isotropic levels of deformations in the test range, extensive deformation up to 15% was seen in the lower stress ranges (0–0.025 MPa). Then, the strain of both directions increased gradually from 15% to 25% in the stress range of 0.025–0.1 MPa. Finally, the sudden increase (25–35%) of both the directional stresses was recorded in the short range of high stress (0.1–0.7 MPa) as an indication to move toward a deformational limitation. In alignment with the computational modeling results, the T/L modulus ratio (1.45) of BMR mesh was matched with that of abdominal wall tissue while the others ranged around a ratio of 1.

The elasticity preservation of BMR mesh was examined under continuous movement with resistance to degradation. Both T



and L directions of the BMR mesh maintained a consistent stress level (ratio to the average stress of test samples) under 20 000 cyclic strains like those of ADM and PP (Figure S4a, Supporting Information). Together, this indicated the promising stability to fatigues in response to continuous abdominal movement. The 6-month degradation of BMR mesh was at maximum 7.8% of weight loss (Figure S4b, Supporting Information), which was comparable with non-degradable PP (maximum 1%), as determined using the accelerated aging condition according to ASTM 1980. The stress-relaxation ratios for BMR mesh to L and directions exhibited no significant differences with those of PP mesh (Figure S4c, Supporting Information) as supported by the slope of the stress decrease, indicating the long-term stability of BMR mesh to the PP level.

2.4. Concept and Thermomechanical Parameters to Configure the Shape of BMR Mesh

Polymeric medical devices offer advantages including biocompatibility, biodegradability, and tunable mechanochemical properties in addition to a drug loading option.^[29] Continuous progress has been made in developing innovative medical devices by advancing the polymer properties to operate the body function following a shape change-mediated guidance.^[30] In this study, the thermomechanical properties of the polymer were tuned to enable in situ shape configuration upon device implantation to adapt and change the structure in response to the anisotropic abdominal movement. The shape configuration of flat mesh follows the given logic, i.e., i) The semicrystalline property of PCL/PCL-PGMA polymer with reduction in T_m (51 °C) upon cross-linking (Figure 2a). ii) Saline, warmed up to 43 °C so that the heat damage to tissues can be minimized. When the mesh is treated with warm saline, the polymer chains start to absorb heat energy (E) and become flexible because the chain mobility increases. iii) The incubation of mesh in the warm saline results in decrystallization of polymer chains because of heat E accumulation iv) so that the mesh can be molded onto a tissue shape by applying forces

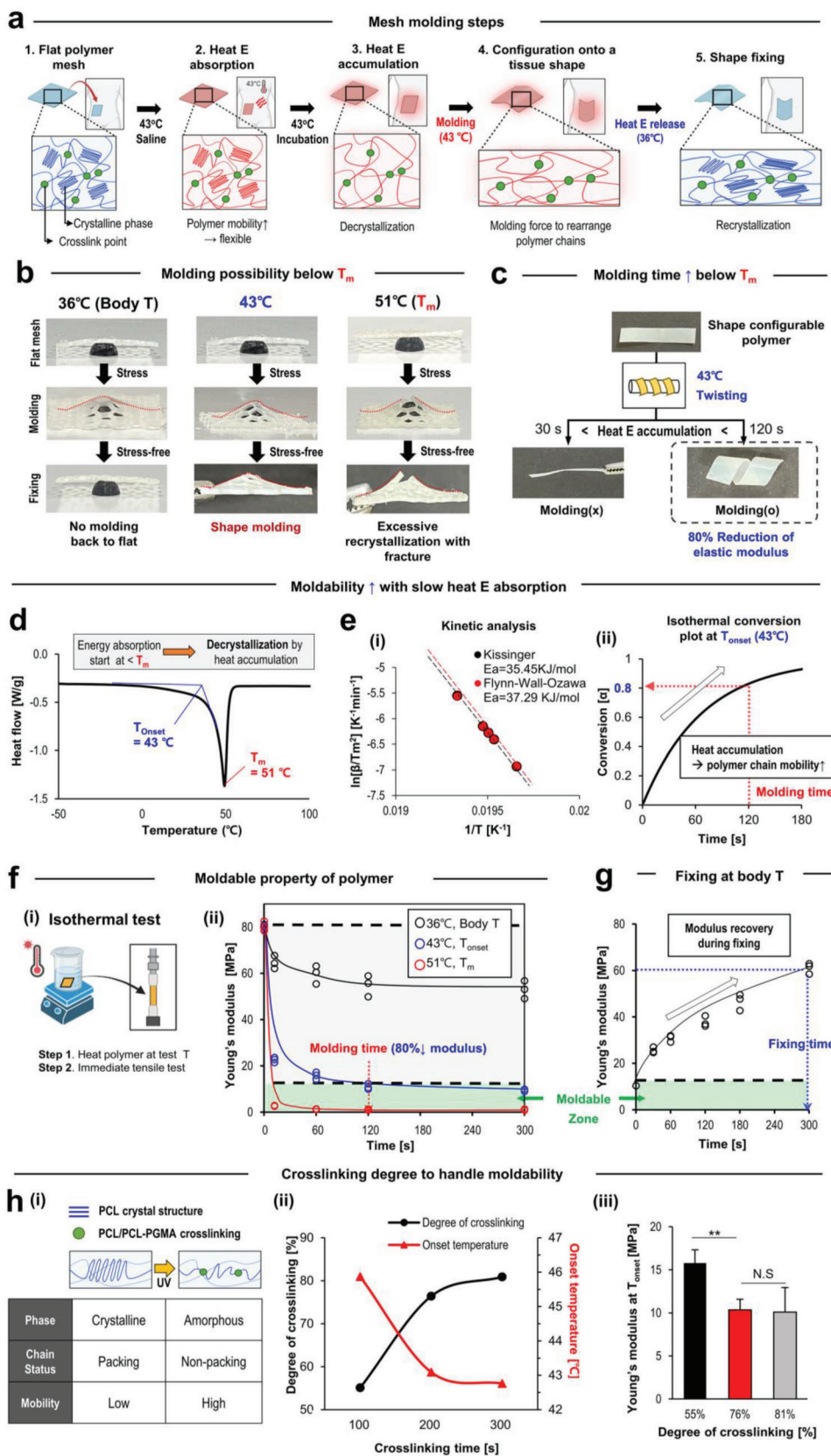
to rearrange the polymer chains. v) As the saline is cooled down to 36 °C, the polymer chains undergo recrystallization to enable shape fixing.

Mesh molding below T_m (43 °C) resulted in superior shape fixing compared to no molding as heat E accumulation at 36 °C was insufficient. The fracture generation at T_m (51 °C) with excessive recrystallization was driven likely because of the fast release of heat E (Figure 2b). Resultingly, the molding possibility and superiority at 43 °C (below T_m) were confirmed (Figure 2c), and 43 °C was defined as T_{onset} . Molding at T_{onset} required 120 s of heat E accumulation to reduce 80% of elastic modulus as an indication of enough chain flexibility to configure a shape by force. When the heat energy absorption lasted only for 30 s, the reduction of elastic modulus did not reach 80%, thereby confirming the result.

2.5. Non-Isothermal and Cross-Linking Properties of BMR Mesh

The endothermic heat transfer that started at T_{onset} (43 °C) as an indication of gradual heat E accumulation into the polymer chains provided the confirmational evidence through the non-isothermal melting test using DSC (Figure 2d). Kinetic analysis was employed to validate that the polymer crystallinity decreased as the heat E accumulated into BMR mesh (Figure 2e). i) The results of non-isothermal melting analysis were used to calculate activation energy, Arrhenius exponent, and reaction order by plotting changes of $\ln[\beta/T_m]$ as a function of $1/T$ following Kissinger and Ozawa equation (T : Temperature, T_m : melting temperature, β : melting rate). ii) Consequently, as the endothermic reaction time increased isothermally under 43 °C, the reduction of PCL/PCL-PGMA crystallinity (conversion (α)) exponentially increased to reach 80% for 120 s. Because the conversion (α) moved to a lag phase afterward, the molding condition was set at 120 s of incubation at 43 °C with 80% reduction of crystallinity. The incremental heating rate during non-isothermal melting of PCL/PCL-PGMA increased the endothermic heat flow

Figure 1. Design validation of body motion responsive (BMR) mesh. a) The stiff T and elastic L motion of abdomen justifies the need of anisotropic stiffness in the mesh design. b) *Ex vivo* directional tissue stiffness. i) Schematic representation of *ex-vivo* tensile test of rat abdomen tissue. ii) Stress-strain curves of the anterior abdominal wall were obtained by dynamic mechanical analysis (DMA). iii) The *ex vivo* tensile test using rat abdomen tissues post-harvesting revealed 1.45 times the stiffness in the T modulus over the L direction. c) i) Experimental design for assessing polymer fatigue accumulation during daily movement. In vivo directional motion of tissue was confirmed by setting real-time accumulation of two directional fatigues into the polymer films upon attachment onto the rat abdomen. ii) As a result of fatigue accumulation, the samples that moved farther exhibited earlier failure in response to cyclic strains as the cycle to failure decreases significantly from no motion to the T and further in the L direction films. d) As a single unit model of BMR mesh, i) a string was added to the T direction of each honeycomb unit (isotropic base) following the concept that engineering microstructure of each of repeated units can tailor the physical properties of the whole structure.^[27,28] The BMR mesh was designed to play the role of bowstring that produces the stretch-dominant (T) stiff and bending-dominant (L) elastic properties, thereby operating the anisotropic directional functions to shoot arrows. As a result of T string addition, ii) the anisotropic distribution of directional modulus is generated in the single unit compared to the isotropic distribution of honeycomb unit in the computational modeling. iii) In the further modeling analysis of tensile modulus with a polar chart, the T direction of a single anisotropic unit was 6.9 times stiffer than the L direction in contrast to the no directional difference of modulus in the isotropic single unit. Then, e) when the single units are rearranged in repeated patterns, the model pattern exhibiting the 1.45 T/L modulus ratio is determined in alignment with the *ex vivo* analysis of abdomen wall tissues. i) As candidates, anisotropic repeated patterns (1-3 and Triangle) are generated through 2D spatial rearrangements of the honeycomb microstructure (isotropic base), followed by calculating the distribution of directional modulus of each pattern. ii) When the T/L modulus ratio is analyzed, the ratio of repeated pattern 3 of a single anisotropic unit decreases from 6.9 to 1.43, in close alignment with ratio of abdominal wall (1.45), thereby serving as the pattern for BMR mesh. f) The experimental validation of the pattern effect is carried out i) through tensile tests on acellular dermal matrix (ADM, commercial control) and sample meshes with honeycomb (isotropic control) versus anisotropic BMR pattern. ii) The T and L directions of both honeycomb and BMR meshes exhibit nearly linear relationships between stress and strain, indicating a predictable deformation up to 35% by controlling the stress. Only the stiff BMR-T requires more stress (i.e., anisotropic factor) to deform to the same level as others (BMR-L, honeycomb-T and L) whose levels of stress-strain changes are similar throughout the test range. iii) In alignment with the computational modeling results, the T/L modulus ratio (1.45) of BMR mesh is matched with that of the abdominal wall tissue while the ratio of others ranged around 1. $**p < 0.01$ and $***p < 0.001$ ($N = 5$ each group). (These figures were created with Biorender.com).



with maintenance of T_m in DSC analysis (Figure S5 and Table S1a, Supporting Information).

The molding condition was confirmed by the following: i) Analyzing decremental tensile modulus due to incremental chain mobility upon heat E accumulation under isothermal incubation at test temperatures (36, 43, and 51 °C) (Figure 2f). ii) The incubation at 43 °C for 120 s led to 80% reduction of modulus from 80 MPa to below 15 MPa in contrast to the insufficient reduction (>50 MPa) at 36 °C and too fast drop (<30 s) to nearly zero at 51 °C. As shape fixing was set by decreasing T from 43 °C to 36 °C for 300 s, the heat E was released with recrystallization of polymer chains, resulting in the gradual recovery of modulus up to 60 MPa (Figure 2g). Crystallization kinetics of PCL/PCL-PGMA was analyzed using differential scanning calorimetry (DSC) in a non-isothermal status by varying the cooling rate (explained in Supporting Information). The incremental cooling rate increased the exothermic heat flow with the maintenance of T_c range in DSC analysis (Figure S6a and Table S1b, Supporting Information). Avrami plots of crystallinity $X(t)$ were modified as a function of t so that the crystallization rate constant (k_a) and Avrami exponent (n_a) were calculated through the slope and the intercept value (Figure S6b and Table S1c, Supporting Information). The Avrami exponent value was between 2 and 3 with no significant difference under various cooling rate conditions, indicating 2D growth of crystallization behavior. No changes in the patterns of Wide X-ray Diffraction (WXR) patterns between the recovery and original shapes indicate maintenance of crystal structure during shape configuration (Figure S6c, Supporting Information).

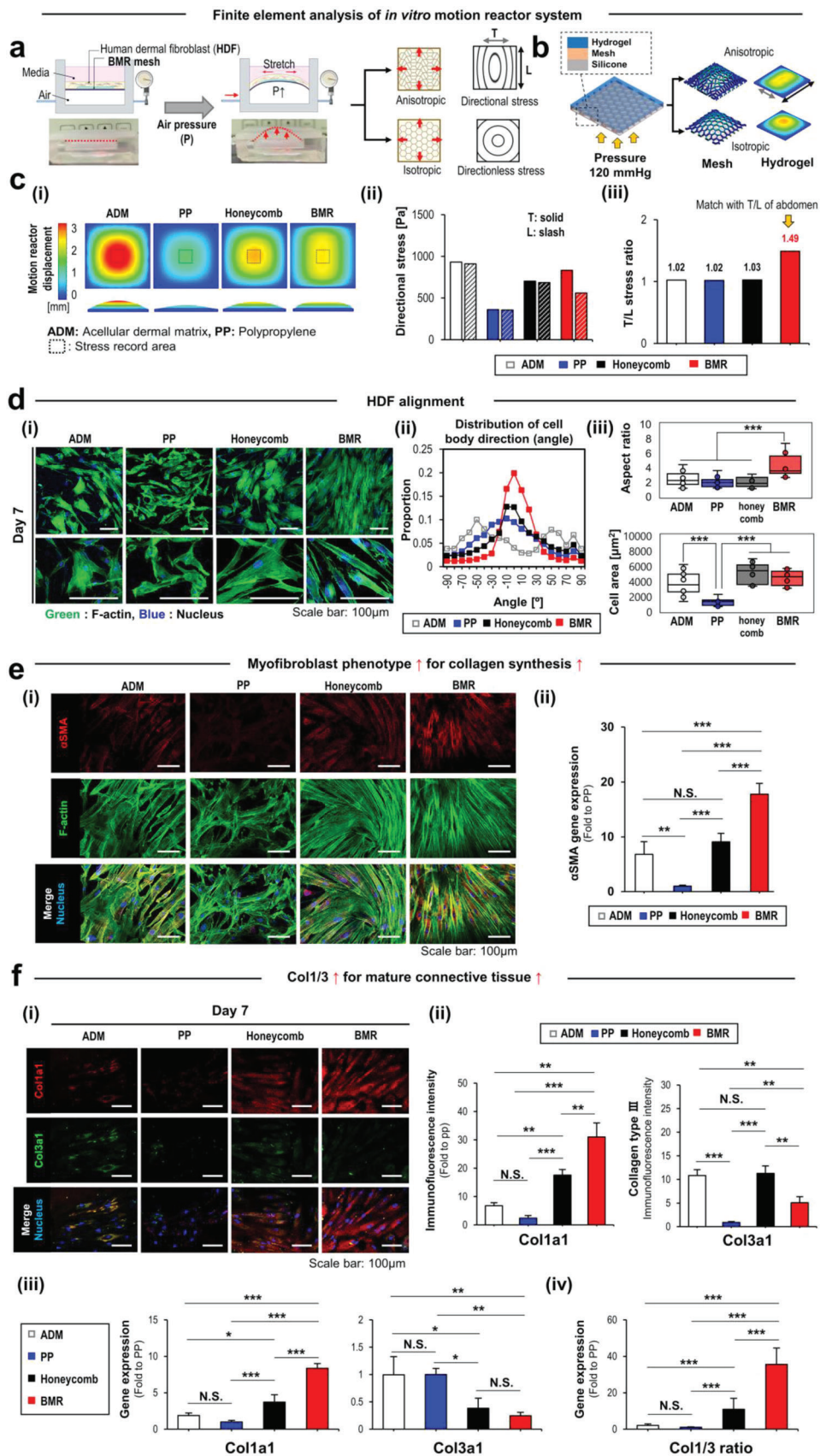
PCL/PCL-PGMA underwent cross-linking in inner-polymer chains (Figure 2h), thereby i) converting packed crystalline phases to the unpacked amorphous status, so that the chain mobility increased. ii) Consequently, as the heat E rearranged polymer chains decrease because of the incremental chain mobility, the incremental cross-linking time results in a decrease in T_{onset}

as opposed to the degree of cross-linking. iii) Along the same line, as the degree of cross-linking increased from 55% to more than 76%, the corresponding modulus decreased significantly, but with no significant decrease in modulus between 76% and 81% of cross-linking degree. The cross-linking time was determined to be 200 s upon UV irradiation to preserve the maximum elasticity of PCL-PGMA (Figure S7, Supporting Information). The excessive cross-linking time over 200 s reduces the maximum strain likely because of recrystallization by UV heating.

2.6. In Vitro Motion Reactor System with Fibroblast Culture under Handling of Anisotropic Stress by BMR Mesh

The motion reactor was designed to utilize air pressure-based cyclic intumescence from the bottom like an abdominal motion (Figure 3a and Figure S8, Supporting Information). A silicone membrane was placed and sealed in the air space to synchronize with the cyclic intumescence as air was injected and deflated. Then, a test mesh was adhered onto the silicone through gluing gelation of gelatin hydrogel, which also promoted the attachment of human dermal fibroblasts (HDFs) so HDFs could be exposed to the cyclic intumescence during 7-day culture. The directional stress (T/L ratio) of the hydrogel on anisotropic BMR versus isotropic honeycomb mesh was analyzed using Finite element analysis (FEA) by applying 120 mm Hg pressure mimicking the inter-abdominal deployment (Figure 3b). In response to the cyclic intumescence of bioreactor (Figure 3c), i) FEA validated that only BMR mesh exhibits anisotropic T/L displacement compared to only centralized high inflation of acellular dermal matrix (ADM), small displacement of stiff polypropylene (PP), and isotropic decentralized displacement of honeycomb with low inflation. This result was confirmed ii) by the high T/L stress ratio of BMR mesh compared to other groups. iii) As a result, 1.49 T/L

Figure 2. Thermomechanical property of BMR mesh to configure a shape. a) Schematic representation of the shape molding steps during hernia repair mesh implantation. The shape configuration of flat mesh utilizes i) the semicrystalline property of PCL/PCL-PGMA polymer with the reduced T_m (51 °C) upon cross-linking. ii) Saline is warmed up to 43 °C so that heat damage to tissues can be minimized. When the mesh is treated with the warm saline, the polymer chains start to absorb heat energy (E) and become flexible because the chain mobility increases. iii) The incubation of mesh in the warm saline results in decrystallization of polymer chains due to heat E accumulation iv) so that the mesh can be molded onto a tissue shape by applying forces to rearrange the polymer chains. v) As the saline is cooled down to 36 °C, the polymer chains undergo recrystallization to enable shape fixing. b) Mesh molding below T_m (43 °C) results in superior shape fixing compared to no molding with insufficient heat E accumulation at 36 °C and fracture generation at T_m (51 °C) with excessive recrystallization likely due to fast release of heat E . Hence, the molding possibility and superiority at 43 °C (below T_m) are confirmed, and 43 °C is defined as T_{onset} . c) Molding at T_{onset} requires 120 s of heat E accumulation to reduce 80% of elastic modulus as an indication of sufficient chain flexibility to configure a shape by force. On the other hand, when heat energy was absorbed at 43 °C for 30 s, shape molding did not occur due to insufficient reduction of elastic modulus. d) As a confirmational evidence in the non-isothermal melting test using DSC, the endothermic heat transfer starts at T_{onset} (43 °C) as an indication of gradual heat E accumulation into the polymer chains. e) The kinetic analysis is used to validate that the polymer crystallinity decreases as the heat E is accumulated into BMR mesh. i) The results of non-isothermal melting analysis are used to calculate activation energy, Arrhenius exponent, and reaction order by plotting changes of $\ln[\beta/T_m]$ as a function of $1/T$ following Kissinger and Ozawa equation (T : Temperature, T_m : melting temperature, β : melting rate). ii) Consequently, as the endothermal reaction time increases isothermally under 43 °C, the reduction of PCL/PCL-PGMA crystallinity [conversion (α)] exponentially increases to reach 80% for 120 s. Because the conversion (α) moves to a lag phase afterward, the molding condition is set as 120 seconds incubation at 43 °C with 80% reduction of crystallinity. f) The molding condition is confirmed by i) analyzing decremental tensile modulus due to incremental chain mobility upon heat E accumulation under isothermal incubation at test temperatures (36, 43, and 51 °C). ii) The incubation at 43 °C for 120 s leads to 80% reduction of modulus from 80 MPa to below 15 MPa in contrast to the insufficient reduction (> 50 MPa) at 36 °C and too fast drop (<30 s) to nearly zero at 51 °C ($N = 3$, each group). g) As shape fixing is set by decreasing T from 43 °C to 36 °C for 300 s, the heat E is released with recrystallization of polymer chains, resulting in the gradual recovery of modulus up to 60 MPa ($N = 3$, each group). h) PCL/PCL-PGMA undergoes cross-linking in inner-polymer chains, thereby i) converting packed crystalline phases to the unpacked amorphous status so that the chain mobility increases. ii) Consequently, as the heat E rearranges, the polymer chains decrease due to the incremental chain mobility, the incremental cross-linking time results in decreases in T_{onset} as opposed to the degree of cross-linking. iii) Along the same line, as the degree of cross-linking increases from 55% to more than 76%, the corresponding modulus decreases significantly, but there is no significant decrease in modulus between 76% and 81% of cross-linking degree. $**p < 0.01$ ($N = 4$ each group, NS: non-significant). (These figures were created with Biorender.com).



ratio of BMR mesh was in alignment with that of abdomen while the ratio for other test groups ranged ≈ 1 .

When viability and proliferation of HDFs were determined after 7-day culture on the motion reactor, PP lowered cell viability significantly compared to the other test groups, and BMR showed the highest cell proliferation among the test groups (Figure S9a,b, Supporting Information). Anisotropic mechanical stress of BMR mesh promoted HDF alignment in support by the same directional distribution of actin fibers (Figure 3d) i) as shown by immunostaining F-actin and nucleus. Consequently, ii) the cell body direction was distributed in the narrowest range in BMR mesh as an indication of most cell alignment in contrast to the bipolar distribution of ADM and relatively broader ranges of the distribution in honeycomb and PP. iii) This result was supported by the highest aspect ratio of HDFs in BMR mesh compared to the other test groups. BMR mesh maintained the HDF areas to the similar levels to that of ADM and honeycomb, but stiff PP showed a significant decrease in the area, indicating poor cell health.

As an indication of healthy regeneration of the abdomen tissue (Figure 3e), a myofibroblast phenotype of HDFs was induced significantly by BMR mesh when compared to the other test groups, as determined by the expression of alpha-smooth muscle (α SMA) i) at protein and ii) gene levels by immunostaining and PCR, respectively. The stiff PP lowered the expression levels significantly compared to the others. Hernia repair can be prevented by promoting the expression of mature collagen type 1a1 (Col1a1) as opposed to immature Col3a1^[20] (Figure 3f) and as shown by BMR mesh compared to the other test groups i) in immunostaining with ii) quantitative analysis. iii) This result was further supported by the gene expression of Col1a1 and Col3a1, resulting in iv) the highest Col1/3 ratio in BMR mesh compared to others.

2.7. Rat Abdominal Hernioplasty to Validate Regenerative Effects

The rat abdominal hernioplasty with deployment of mesh samples enabled determination of vascularization and Col1/3 ratio as healthy regeneration factors at day 14 upon sacrifice (Figure 4a). The model was constructed by incising and defecting (0.5 cm \times 0.5 cm) of abdominal wall (Figure 4b; Movie S1, Supporting In-

formation). Then, BMR mesh was placed to cover the defect, followed by treatment and incubation (120 s) of warm saline (43 °C) so that the mesh could absorb heat and thereby be molded to fit into the abdominal shape. After implantation for 14 days (Figure 4c), the test groups (No mesh, honeycomb mesh, and BMR mesh) were used to determine blood vessel formation i) by histology with CD31 immunostaining (Figure 4d). ii) The number of vessels and iii) vasculogenic gene expression (CD 31, KDR, and vWF) increased significantly from No mesh to honeycomb and further to BMR mesh. The structural stability of mesh was maintained after supporting the anisotropic movement of the abdomen for 14 days, as evidenced by over 90% consistence rates of mesh pattern angles between the day 0 and 14 images (Figure S10, Supporting Information).

During 14-day implantation in the model of rat abdominal hernioplasty (Figure 5a), BMR mesh exhibited superior function compared to No mesh and honeycomb mesh in promoting i) collagen alignment by image analyses (vector field analysis and color mapping survey) of Masson Trichrome and Picro sirius red staining with ii) a significant increase in Col1a1 production as opposed to Col3a1. iii) Consequent highest ratio of Col1/3 in BMR mesh indicates promising potential to prevent hernia recurrence most efficiently among the test groups. This result was further confirmed by i) immunofluorescence staining of Col1a1 and Col3a1 with ii) quantitative analysis of Col1/3 ratio and iii) their gene expression by PCR (Figure 5b). The protective collagen characteristics accompanied the phenotypic change of fibroblast to myofibroblasts i) by immunostaining with ii) quantitative analysis to the highest ratio of myofibroblast (α SMA+) to fibroblast (Vimentin+) in BMR mesh in addition to iii) the highest gene expression of α SMA compared to the other test groups (Figure 5c).

3. Discussions

In this study, BMR mesh was suggested as an instructive solution to promote the hernia repair process. The polymeric mesh is classified to knitted mesh and woven fabric, and the knitted mesh is known to exert an anisotropic property.^[1] It was reported that the anisotropic property of hernia mesh influenced the surgical outcomes depending on the orientation of implantation.^[31]

Figure 3. In vitro motion reactor system with fibroblast culture under handling of anisotropic stress by BMR mesh. a) The motion reactor utilizes air pressure-based cyclic inflation from the bottom like an abdominal motion. A silicone membrane is placed and sealed in the air space to synchronize with the cyclic inflation as air is injected and deflated. Then, a test mesh is adhered onto the silicone through gluing gelation of gelatin hydrogel which also promotes attachment of human dermal fibroblasts (HDFs) so that the HDFs can be exposed to the cyclic inflation during 7-day culture. b) The directional stress (T/L ratio) of the hydrogel on anisotropic BMR versus isotropic honeycomb mesh is analyzed using Finite element analysis (FEA) by applying 120 mmHg pressure like the situation of inter-abdomen deployment. c) Calculation of directional stress exerted on the motion reactor. In response to the cyclic inflation of bioreactor, i) FEA validates that only BMR mesh exhibits anisotropic T/L displacement compared to centralized high inflation of acellular dermal matrix (ADM), small displacement of stiff polypropylene (PP), and isotropic decentralized displacement of honeycomb with low inflation. This result is confirmed ii) by the high T/L stress ratio of BMR mesh compared to the similar stresses between T and L directions of the other groups, resulting in iii) 1.49 T/L ratio of BMR mesh in alignment with that of abdomen while the other test groups are ranged around ratio of 1. d) Anisotropic mechanical stress of BMR mesh promotes HDF alignment in support by the same directional distribution of actin fibers i) as shown by immunostaining F-actin and nucleus. Consequently, ii) the cell body direction is distributed in the narrowest range in BMR mesh as an indication of the highest cell alignment in contrast to the bipolar distribution of ADM and relatively broader ranges of distribution in honeycomb and PP. iii) This result is supported by the highest aspect ratio of HDFs in BMR mesh compared to the similar levels of aspect ratio in other test groups. BMR mesh maintains the HDF areas to the similar levels of ADM and honeycomb but stiff PP shows a significant decrease in the area, indicating poor cellular health. e) As an indication of healthy regeneration of the abdomen tissue, a myofibroblast phenotype of HDFs is induced significantly by BMR mesh compared to the other test groups as determined by the expression of alpha smooth muscle (α SMA) i) at protein and ii) gene levels by immunostaining and PCR, respectively. The stiff PP lowers the expression levels significantly compared to the others. Hernia repair can be prevented by promoting the expression of mature collagen type 1a1 (Col1a1) as opposed to immature Col3a1^[20] as shown by f) BMR mesh compared to the other test groups i) in immunostaining with ii) quantitative analysis. iii) This result is further supported by the gene expression of Col1a1 and Col3a1, resulting in iv) the highest Col1/3 ratio in BMR mesh among others. * $p < 0.05$, ** $p < 0.01$, and *** $p < 0.001$ (N = 4, each group, NS: non-significant).

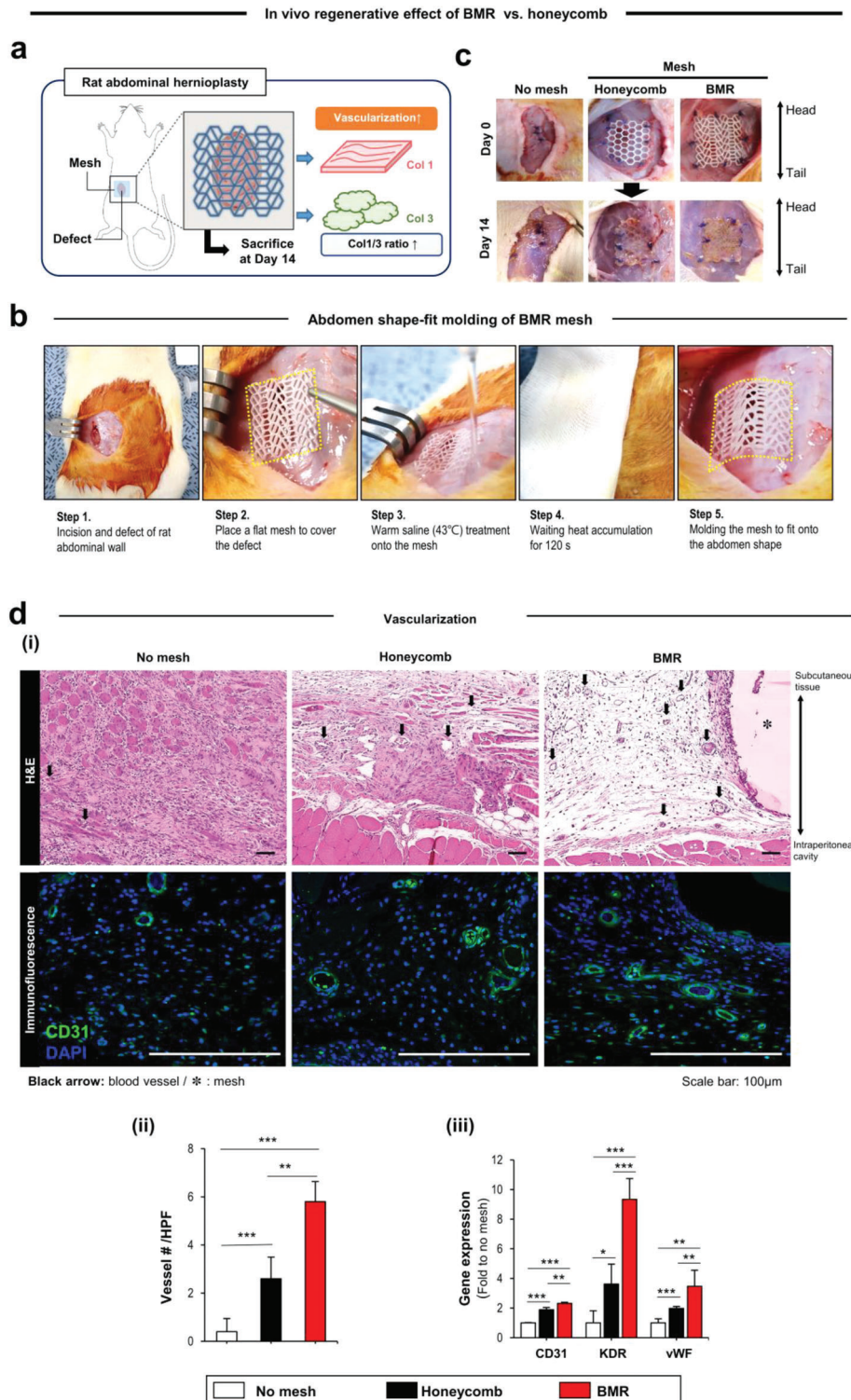
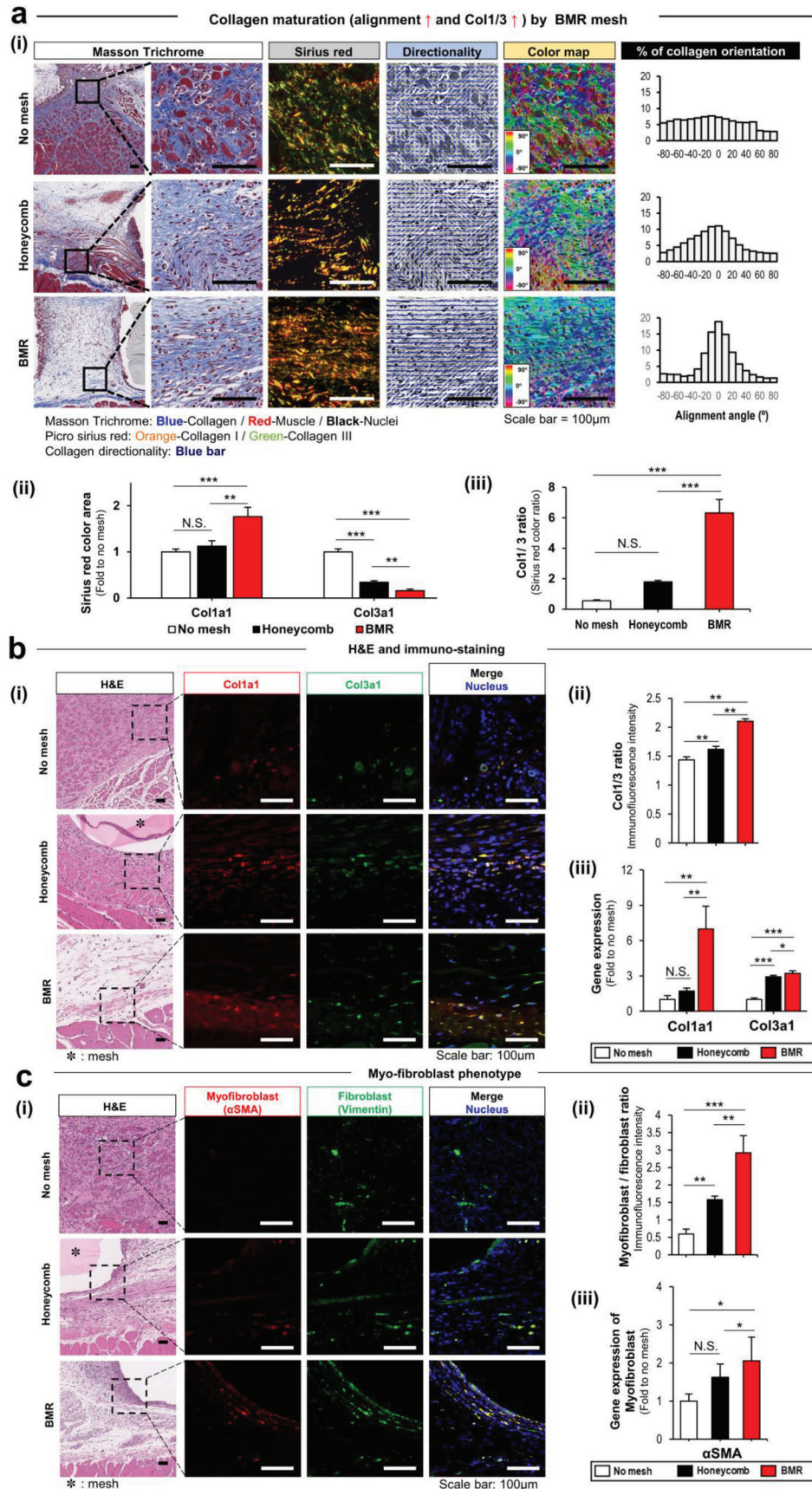


Figure 4. Rat abdominal hernioplasty to validate regenerative effects of BMR mesh with shape molding. a) The rat abdominal hernioplasty with the deployment of mesh samples enables determination of vascularization and Col1/3 ratio as healthy regeneration factors at day 14 upon sacrifice. b) The model is constructed by incising and defecting (0.5 cm × 0.5 cm) of abdominal wall. Then, BMR mesh is placed to cover the defect, followed by treatment and incubation (120 s) of warm saline (43 °C) so that the mesh can absorb heat and thereby be molded to fit into an abdomen shape. c) After implantation for 14 days, the test groups (No mesh, honeycomb mesh, and BMR mesh) are used to determine blood vessel formation i) (black arrow) in histology with CD31 immunostaining. ii) The number of vessels per high power field (HPF) and iii) vasculogenic gene expression (CD31, KDR, and vWF) increase significantly from No mesh to honeycomb and further in BMR mesh. **p* < 0.05, ***p* < 0.01, and ****p* < 0.001 (N = 5, each group).



However, there is an unmet need in suggesting a clear design strategy to synchronize the anisotropic movement between target organ and device, representing the value of our approach. The basic design was approached following the concept that the mechanical properties between implanted devices and target tissue should align to prevent stress concentration around the wound site, and thereby facilitate the regenerative response.^[12] As the most significant point, the unique collaboration of mesh design with polymer properties could handle the anisotropic abdomen motion efficiently as evidenced by the promotion of regenerative effect on hernia repair. With the starting point, we determined the motion-related anisotropic property of abdomen tissue to be 1.45 T/L ratio. This anisotropic abdominal motion was also confirmed by fatigue accumulation to PLA films post attachment to T and L directions of abdomen motion. Moreover, the series of results including the modulus match (Figure 1e(ii),f(iii)), in vitro ADM and honeycomb versus BMR mesh (Figure 4), and in vivo honeycomb versus BMR mesh (Figure 5) indicates that the modulus match between BMR mesh and abdominal tissue supported the healthy fibroblast actions, and tissue regeneration as opposed to the mismatched ones (i.e., ADM and honeycomb). These results have never been elucidated and applied to mesh design, representing a breakthrough in foundation of the present design strategy. Also, this approach plays an instructive role in developing other implantable devices considering the fact that every body part is constructed and moves in an anisotropic manner.

The hypothesis was that the anisotropic motion synchronization between the abdominal wall and BMR mesh improves the regenerative effect on hernia repair. As a result, the design was approached by progressing from theory to computational calculation and further to experimental validation. The single structural unit was analyzed based on Maxwell's criterion to convert the isotropic honeycomb by adding a string, thereby justifying the arrow string mode as a foundation to develop an isotropic unit. The single units were rearranged to decide the repeated pattern that exhibited and matched T/L ratio with the abdominal wall as validated by computational calculation and mechanical tests using the polymer samples. In particular, the number of lines per joint was analyzed as a determinant factor of structural stiffness in the mesh design so that the final decision could be supported by the calculated modeling prediction. The cooperative approach provides an instructive guideline to use FEA in support of experimental validation for upgrading isotropic designs to existing medical devices. In this way, the limitation of prevalent uniform designs with consistent material properties can be overcome leading to improved clinical efficacy.

As a result, the polymer was chosen based on its thermomechanical properties, as it can be modified to meet each specific purpose even in the same device. Also, BMR mesh was proposed to enable molding onto the target abdominal struc-

ture such that the disturbance of motions between the abdominal wall and mesh could be minimized, justifying the need for unique polymeric properties in addition to the specific structural design. PCL is a semicrystalline polymer; thus, its chain mobility increases upon temperature shifts, resulting in the reduction in the stiffness with decrystallization process. At this point, the polymer becomes ready for molding and then moves to recrystallization upon heat release so that the molded structure can be fixed. However, because proteins get denatured at 50 °C thus, abdominal tissues are at risk to be damaged—the alteration of chain mobility must be set to occur below 50 °C by cross-linking. Therefore, 96%PCL–4%PGMA was used to process inter-chain cross-linking because PGMA (cross-linking point) spreads inside PCL chains such that the cross-linking also reduces T_m together with crystallinity as reported previously.^[23] As an additional benefit, the inter-chain cross-linking enabled tight holding of polymer chains, thereby maintaining the basic structure of surgical mesh even upon temperature shift to near T_m .

However, because the stiffness of PCL-PGMA was not enough to prevent the internal organs from protruding outward, the polymer structure was modified to six arms so that the network force could be improved. Furthermore, 6arm-PCL was blended with PCL to increase the stiffness relying on the crystallinity of pure PCL as the final form of 6arm-PCL/PCL-PGMA. This material strategy resulted in the step-by-step improvement to provide sufficient stiffness as a form of hernia mesh in dealing with even the peak pressure of abdominal motion. Next, the parameters of shape molding were determined to enable anisotropic motion synchronization. As a result, the kinetic analyses of non-isothermal crystallization and crystal growth behavior were carried out using the Avrami method with XRD; consequently, the linear growth and stability of the crystal structure were identified (Supporting Information).^[32–34] The analytical results of non-isothermal melting and kinetics through the Kissinger^[35] and the Flynn–Wall–Ozawa (FWO)^[36] methods determined the endothermic reaction time to enable efficient shape molding. The in-depth kinetic analyses of thermomechanical properties serve as a representative example to instruct upgrading the utility of existing medical materials, thereby facilitating implantation and consequent applications of medical devices. So far, shape-configurable polymers have mainly relied on the shape recovery function at a specific temperature. As an advanced strategy of this study, the thermomechanical properties of polymer were tuned to enable *in-situ* shape configuration, thereby handling the heterogeneous environmental stress within the body.

3D printing utilizes a computer-aided design (CAD) software to transfer a device design into material printing through layer-by-layer deposition.^[6] The advantage of our approach is to produce patient-specific devices using clinical CT and MRI

Figure 5. Health regeneration of abdominal connective tissue by BMR mesh to prevent hernia recurrence. During 14-day implantation in the model of rat abdominal hernioplasty, a) BMR mesh exhibits superior functions compared to No mesh and honeycomb mesh in promoting i) collagen alignment by image analyses (vector field analysis and color mapping survey) of Masson Trichrome and Picro sirius red staining with ii) a significant increase in Col1a1 production as opposed to Col3a1. iii) The consequent highest ratio of Col1/3 in BMR mesh indicates promising potential to prevent hernia recurrence most efficiently compared to other test groups. b) This result is further validated by i) immunofluorescence staining of Col1a1 and Col3a1 with ii) quantitative analysis of Col1/3 ratio and iii) their gene expression by PCR. c) The protective collagen characteristics accompanies the phenotypic change of fibroblast to myofibroblasts i) in immunostaining with ii) quantitative analysis to revealing the highest ratio of myofibroblast (α SMA+) to fibroblast (Vimentin+) in BMR mesh in addition to iii) the most gene expression of α SMA compared to the other test groups. * $p < 0.05$, ** $p < 0.01$, and *** $p < 0.001$ ($N = 5$, each group, NS: non-significant).

images.^[37] Additionally, 3D printing enables post-modifications such as drug coating^[16] and cell embedding,^[38] thereby serving as one of the most versatile technologies for a wide range of applications. In this study, 3D printing was used to tune the mesh structure by testing the suggestions from computational modeling. As another advantage, the structures were used to create PDMS molds where PCL/PCL-PGMA polymer was poured and cross-linked, thereby simplifying the process of device fabrication. When the single unit of mesh was designed, the Maxwell stability criterion was used to determine the structural stability of 2D mesh design in a strut-joint model.^[28] The stability criterion was given by $M = b - 2j + 3$, where M represented structural stability, b was the number of struts, and j was the number of joints (Figure S1a, Supporting Information). In the honeycomb structure (Figure 2b), the structural stability was $M = -3$ with a bending-dominant property, which became -2 upon string addition, resulting in a partial bending property. In contrast, M of triangular structure exhibited was 1, indicating a stretch-dominant property. However, this single unit stability did not fully reflect the mechanical properties of mesh macrostructure. Hence, the macroscopic stiffness was adjusted by arranging the panel design of a single unit connection, and the connectivity rule played a major role in determining the stiffness by varying the number of struts in connection with each single joint. The required stiffness was obtained by maintaining the joint connectivity (Z) ≥ 4 and 6 in two- and three-dimensional models, respectively. Together, the anisotropic mechanical properties were adjusted by altering the arrangement of single units and the corresponding Z number.

In this study, we presented another instructive model to carry out in vitro examination before moving to the challenging animal study. The motion reactor was developed to simulate the abdominal motion through the computational modeling analyses of design with the easy fabrication procedure. The system enabled culturing HDFs under the physiological cyclic pressure upon abdominal motion; thus, the regenerative effect of BMR mesh was elucidated in promoting ECM synthesis through the phenotypic change of HDFs to myofibroblasts. In the rat hernioplasty model, the ECM synthesis was driven to repair the hernia with healthy connective tissue as the production of mature Col1 increased as opposed to the immature Col3. Also, these repair processes were supported by the vascularization around the surgical site, thereby proving the hypothesis. Previous studies have reported that the programmable changes of device shape can modulate cell adhesion, proliferation, and viability under cell-material interaction.^[39,40] The BMR mesh exhibited configurable shape changes due to the thermo-responsive dynamics in the polymer chain mobility. In both the in vitro motion reactor experiment and in vivo model, the collaboration between the polymer properties and mesh design directed the anisotropic synchronization with the abdomen movement. As a result, the actin and morphology alignment of human fibroblasts were induced, suggesting that the anisotropic movement can instruct the cellular behavior in agreement to a previous study.^[41]

The novelty of the present study lies in the fact that the anisotropic movement of the abdomen was synchronized with BMR mesh under implantation, thereby suggesting a considerable solution to prevent hernia recurrence. This novelty was gen-

erated by analyzing the influence of mesh patterns to support the movement and regeneration of abdominal tissue. Moreover, the thermomechanical properties of the polymer were tuned to exert the synergistic action with the pattern design in addition to the downshift of configuration temperature for user-friendly deployment. The approach of the present study provides an inspirational foundation to consider a new design paradigm of other medical devices for anisotropic motion-prone organs. The key point is that the shape configuration of a mesh device could handle the heterogeneous structural and stress changes within the body.

As points of future study, a mathematical calculation of the relationship between the mesh geometry and mechanical property would strengthen the overall approach of the present study. Previously, a pioneer work elucidated the deformation mechanisms of single hexagonal cell units upon subjecting to various stress directions.^[42,43] As a result, an effective elastic modulus of a single unit structure was derived to improve the mechanical properties of the device in a honeycomb model. However, such mathematical approaches possess limitations in calculating the anisotropic mechanical properties of patterned macrostructure under external loading to diverse directions due to the heterogeneous distribution from surrounding dynamic stresses with non-uniform tissue supports. Instead of the mathematical calculation, this study approached computational modeling with the finite element method to predict the mechanical properties, followed by experimental verification. Despite the meaningful outcomes, further efforts are required to set up the controllability of mechanical properties by varying other parameters (e.g., strut size, length, thickness, angle, etc.), thereby suggesting the next version of mesh design. Also, finite element analyses of the unexplored design parameters validation should be carried out by monitoring the BMR mesh performance in large animals for realistic translation.

4. Experimental Section

Animals: All rat experiments were performed in accordance with the National Institute of Health and approved by the Ethics Committee and the Institutional Animal Care and Use Committee of Yonsei University, College of Medicine (IACUC Approval number, 2020-0080). Sprague Dawley (SD) rats (12 weeks old, female, Orient Bio, Seoul, Republic of Korea) were used for the follow-up experiments.

Anisotropic Mechanical Properties of Rat Abdominal Tissue: The anisotropic properties of the rat abdominal wall were examined regarding differences in the mechanical properties between the transverse (T) and longitudinal (L) directions. Rats were anesthetized with intramuscular injection of zoletil (50 mg kg⁻¹, Zoletil, Virbac Korea, Seoul, Republic of Korea) and xylazine (10 mg kg⁻¹, Rompun, Bayer Korea, Seoul, Republic of Korea). The anterior-lower abdominal wall (1 cm interval from the midline) of each rat was incised, followed by harvesting a wall tissue (1 cm × 1 cm) with the full thickness from the fascia to the muscle layer. The tissue was immediately immersed in PBS, and a tensile test was performed within 1 h after surgery to prevent changes in tissue properties. The mechanical properties between the L and T directions were measured through dynamic mechanical analysis (DMA; DMA 850, TA instrument Inc. New Castle, DE, USA) at a rate of 5 mm min⁻¹ (N = 5, each group).

Anisotropic Movement of Rat Abdominal Wall: The abdominal tissue movement results in the accumulation of anisotropic fatigue to test polymer film upon attachment. As a result, a thin polylactic (PLA) polymer film (30 mm length × 3 mm width, 0.2 mm thickness) was 3D printed (Raised3D Pro2, Irvine, CA, USA) and attached to the rat abdominal wall

in either parallel or perpendicular direction to the head-tail line for 3 days with tegadum (3M, Minnesota, USA) dressing to keep the rat from removing it. As fatigue was accumulated by rat abdominal movement for 3 days, the PLA film was peeled off and subjected to DMA with determining the cycle number to break the films by applying 4.5 N with 50 Hz ($N = 5$, each group).

Finite Element Analysis (FEA) for Mesh Design: The 3D mesh models were designed by FEA in conjunction with CAD programming (version 2018, Autodesk, California, USA), followed by simulation of stress distribution in response to directional displacement using ANSYS mechanical APDL software (ANSYS 2020R1, ANSYS, Canonsburg, PA, USA). As computational modeling requires the input of the physical properties, elastic modulus (78 MPa) and yield strength (7.9 MPa) of PCL-PGMA were provided through the tensile experiment (Figure S3, Supporting Information) with curve fitting following a bilinear isotropic model. Then, tensile simulation was carried out by determining the von Mises stress along the tensile length of T and L directions in test single units and patterned meshes, thereby calculating the T/L modulus ratio.

Polymer Synthesis: The shape configurable polymer was synthesized using ring-opening polymerization of ϵ -caprolactone (CL; 704067, Sigma-Aldrich, St. Louis, MO, USA) and glycidyl methacrylate (GMA; 779342, Sigma-Aldrich). The initiator (dipentaerythritol, 814810, 0.5 mmol, Sigma-Aldrich) and auto cross-linking inhibitor (hydroquinone, H9003, 2.1 mmol, Sigma-Aldrich) were prepared in a three-necked flask with vacuum drying. Then, distilled CL was added to the flask, and the mixture was stirred at 110 °C for 10 min under submerging in an oil bath, followed by the addition of GMA (21 mmol) to react for another 20 min. Next, a solution (3.5 mmol) of 1,5,7-triazabicyclo [4.4.0] dec-5-ene (TBD; 345571, Sigma-Aldrich) and anhydrous acetonitrile (ACN; 271004, Sigma-Aldrich) was added and the reaction proceeded at 110 °C for 6 h under nitrogen purging. The product was dissolved in chloroform (288306, Sigma-Aldrich), precipitated using cold diethyl ether (Sigma-Aldrich), and dried under vacuum for 24 h. Finally, 6-arm 96%polycaprolactone-co-04%polyglycidyl methacrylate (96%PCL-04% PGMA), was obtained,^[15] followed by enhancing the stiffness by blending with PCL (Sigma-Aldrich) to PCL/PCL-PGMA (10/90 w/w).

Thermal Property of Polymer: Basic thermal properties of PCL/PCL-PGMA were first examined by differential scanning calorimetry (DSC; Discovery DSC25, TA Instruments, New Castle, DE, USA). PCL/PCL-PGMA polymer (4 mg) was prepared in Tzero pan (T191218, T191023, TA instrument), which was heated up to 150 °C at a rate of 10 °C min⁻¹ and cooled for two cycles. The first cycle was used to eliminate the thermal and mechanical history of sample, and the second cycle was used to obtain the results. Second, the properties of non-isothermal crystallization were examined by cooling each sample down to -80 °C by varying the cooling rate. Third, a non-isothermal melting curve was drawn by cooling each sample down to -80 °C, followed by heating up to 150 by varying the heating rate in nitrogen atmosphere. The onset temperature (T_{onset}), end temperature (T_{end}) melting temperature (T_m), crystallization temperature (T_c), melting enthalpy (ΔH_m), and crystallization enthalpy (ΔH_c) were determined using the DSC thermograms.

Kinetic Analysis of Polymer Melting: Conversion (α) defines the decrystallization degree of PCL/PCL-PGMA, the kinetics of which were calculated during the endothermic reaction with increasing the polymer chain mobility using Equations (1) and (2):

$$\alpha = \frac{\int_{T_0}^T (dH_m/dT) dT}{\int_{T_0}^{T_\infty} (dH_m/dT) dT} \quad (1)$$

In Equation (1), T_0 and T_∞ are the onset and end temperatures during melting, respectively, and dH_m/dT is the heat flow rate with exclusion of the baseline. Kissinger's method^[44] was used to formulate the reaction

rate Equation (2) of the polymer crystallinity change by multiplying the reaction rate coefficient $k(T)$ to the function of conversion $f(\alpha)$

$$\frac{d\alpha}{dt} = k(T)f(\alpha) = k(T)(1-\alpha)^n \quad (2)$$

In Equation (2), $\frac{d\alpha}{dt}$ is the rate of reaction, $k(T)$ is the rate coefficient, $f(\alpha)$ is the function of reaction mechanism, and n is the reaction order. Then, $k(T)$ was converted into Arrhenius Equation (3):

$$k(T) = Ae^{-\frac{E_a}{RT}} \quad (3)$$

In Equation (3), A is pre-exponential factor, E_a is activation energy, R is universal gas constant (8.314 J mol⁻¹ K⁻¹), and T is absolute temperature. Subsequently, Equations (2) and (3) were combined to Equation (4):

$$\frac{d\alpha}{dt} = Ae^{-\frac{E_a}{RT}} \times f(\alpha) = Ae^{-\frac{E_a}{RT}} \times (1-\alpha)^n \quad (4)$$

Next, Equation (4) was differentiated into time (t) to formulate Equation (5), in which β is constant heating rate dT/dt :

$$\frac{d}{dt} \left(\frac{d\alpha}{dt} \right) = \left(\frac{\beta E_a}{RT^2} - Ae^{-\frac{E_a}{RT}} \times f'(\alpha) \right) \frac{d\alpha}{dt} \quad (5)$$

At the maximum endothermic energy in the reaction, T becomes T_m , and $\frac{d}{dt} \left(\frac{d\alpha}{dt} \right) = 0$, so Equation (5) was converted to Equation (6):

$$\frac{\beta E_a}{RT_m^2} = f'(\alpha) \times Ae^{-\frac{E_a}{RT_m}} \quad (6)$$

The data (Supporting Information) indicates that the polymer crystallinity was linearly deformed during the heating and cooling process. As a result, the reaction order (n) was assumed to be 1. When the reaction order is 1, $f(\alpha) = 1 - \alpha$, and $f'(\alpha)$ becomes -1 . As the final step of Kissinger's method, β/T_m^2 was calculated by taking the natural logarithm using Equation (7):

$$\ln \left(\frac{\beta}{T_m^2} \right) = \ln \left(\frac{AR}{E_a} \right) - \frac{E_a}{RT_m} \quad (7)$$

As a result, the activation energy (E_a) was obtained by plotting $\ln \left(\frac{\beta}{T_m^2} \right)$ and $\frac{1}{T_m}$. So far, the endothermic reaction was analyzed to calculate the activation energy and pre-exponential factor.

As a double confirmation, the Flynn-Wall-Ozawa (FWO) method was approached to calculate E_a , considering variations in the heating rate (β).^[45] First, $g(\alpha)$ was calculated through the integral conversion of Equation (4) to Equation (8) as follows:

$$g(\alpha) = \frac{A}{\beta} \int_{T_0}^T e^{-\frac{E_a}{RT}} dT = \frac{AE_a}{\beta R} \times p \left(\frac{E_a}{RT} \right) \quad (8)$$

This equation was applied to Doyle's approximation^[36] so that $p \left(\frac{E_a}{RT} \right)$ was linearized to $\frac{E_a}{RT}$ in Equation (9):

$$\ln(\beta) = \ln \left(\frac{AE_a}{R} \right) - \ln g(\alpha) - 5.3305 - 1.052 \frac{E_a}{RT} \quad (9)$$

In this way, the E_a value was double confirmed. Consequently, Kissinger and FWO methods were aligned in showing the linearity between $\ln \left(\frac{\beta}{T_m^2} \right)$ and $\frac{1}{T_m}$ in addition to the small difference in the E_a values, thereby double-checking the reaction order (n) to be 1.

Finally, the decrystallization of polymer during the isothermal melting process was calculated by varying the time using Equation (10) through integration of Equation (4) so that changes of conversion (α) as a function of reaction time (t) were analyzed in a plot as follows:

$$\alpha = e^{-\left(t \times A \times e^{-\frac{E_a}{RT}}\right)} + 1 \quad (10)$$

Mechanical Property of Polymer Under Isothermal and Molding Conditions: PCL/PCL-PGMA films (3 mm width \times 30 mm length, 0.3 mm thickness) were prepared, and the basic stress–strain curves were obtained at a controlled rate of 5 mm min⁻¹ at the room temperature ($N = 5$, each group). Then, the isothermal conditions were set by placing the films at each temperature (51 °C, 43 °C, 36 °C) by varying the incubation time (30, 60, 120, and 300 s). The elastic modulus was determined through a tensile test using DMA at a rate of 5 mm min⁻¹ ($N = 3$, each group). In addition, the recovery of modulus was determined when the film was molded in water at 43 °C for 2 min and moved to 36 °C water for each time (30, 60, 120, and 300 s), followed by measuring the elastic modulus using DMA at a rate of 5 mm min⁻¹ at 36 °C ($N = 3$, each group).

Crystalline Property of Polymer: Wide angle X-ray diffraction (WXR) was used to examine the crystallinity before and after molding of PCL/PCL-PGMA (2 cm width \times 2 cm length \times 400 μ m thickness) to elongate by 50% at T_{onset} with fixing at 36 °C. The crystalline structure was analyzed using HR-XRD (Rigaku, TX, USA) at 1.5406 Å (Cu K α) of X-ray wavelength at 40 kV and 40 mA. The diffraction angle (2θ) ranged from 3° to 70°, and the step time was 5° min⁻¹ ($N = 3$, each group).

Thermomechanical Properties by Varying the Cross-Linking Degree: The cross-linking degree of PCL/PCL-PGMA films (3 mm width \times 30 mm length, 0.3 mm thickness) was improved by increasing the exposure time (100, 200, and 300 s) to UV with 365 nm wavelength at intensity of 265 mJ cm⁻². The degree of cross-linking (%) was determined using Equation 11:

$$\text{Degree of crosslinking} = \frac{m_{\text{final}}}{m_{\text{initial}}} \times 100\% \quad (11)$$

In Equation (11), m_{initial} is the dry mass and m_{final} is the mass after dissolving in *N*-methyl-2-pyrrolidone (NMP; Sigma–Aldrich) for 2 h ($N = 4$, each group). The onset temperature (T_{onset}) of film with each cross-linking percentage during the endothermic reaction was measured using DSC under a non-isothermal melting condition at 10 °C min⁻¹. Also, the corresponding Young's modulus and max strain were measured using the samples by DMA tensile analysis through isothermal heating for 120 s under each T_{onset} condition.

Mesh Fabrication with Mechanical Property: The mesh structures (honeycomb and BMR) were produced using CAD with 3D printing (IMC, Carima, Seoul, Republic of Korea) of the supplier's material to flat (2D) forms, which were molded into polydimethylsiloxane (PDMS; Dow Corning, Midland, MI, USA). PCL/PCL-PGMA was dissolved in *N*-methyl-2-pyrrolidone (NMP; 1 g mL⁻¹, Sigma–Aldrich) at 45 °C and mixed with 0.5% photo-initiator, 2-hydroxy-1-(4-(hydroxyethoxy) phenyl)–2-methyl-1-propanone (Irgacure 2959, Sigma–Aldrich). The PCL/PCL-PGMA solution was injected into the PDMS molds by attaching to a glass post-surface modification.

Then, the cross-linking was proceeded by exposing to UV with 365 nm wavelength at 265 mJ cm⁻² for 200 s, followed by washing in distilled water (DW) at room temperature for 2 days and drying under vacuum for 24 h. The mesh samples (BMR, honeycomb, and ADM, 7 mm length \times 7 mm width, 0.04 mm thickness) were subjected to DMA at a controlled rate of 5 mm min⁻¹ at room temperature in both T and L directions to analyze the stress–strain curves of samples ($N = 5$, each group).

Fatigue and Degradation Properties of Mesh: As commercial controls, ADM and PP meshes were compared with BMR mesh (7 mm length \times 7 mm width) to a fatigue test under 20000 cyclic strain using DMA at 37 °C, followed by determining the stress ratio to the average stress of all sample types.

The degradation property was examined using the accelerated aging test of the American Society of Testing and Materials (ASTM) international standard 1980, with the following Equations (12–14) as defined to calculate the period of real-world-time (RT) equivalent usage:

$$\text{Accelerated Aging Time (AAT)} = \frac{\text{Desired (RT)}}{\text{AAF}} \quad (12)$$

$$\text{Accelerated Aging Factor (AAF)} = Q_{10}^{\left[\frac{(T_{\text{AA}} - T_{\text{RT}})}{10}\right]} \quad (13)$$

$$Q_{10} = 2.0 \quad (14)$$

where Desired (RT) is the desired period of real-time, Q_{10} is the temperature coefficient (degree of material change with increasing temperature), T_{AA} is accelerated aging temperature, and T_{RT} is 37 °C. The mesh samples were incubated in normal saline at 60 \pm 2 °C for 37 days with the calculation of the corresponding 6-month values and weight loss (%) using Equations (15–17):

$$\text{AAF} = 2.0^{2.3} = 4.93 \quad (15)$$

$$\text{AAT} = 180/4.93 = 36.51 \quad (16)$$

$$\left(\frac{m_0 - m_a}{m_0}\right) \times 100\% \quad (17)$$

In Equation (17), m_0 is the initial mass and m_a is the mass after degradation ($N = 4$, each group).

DMA was used to examine the stress relaxation properties of BMR mesh in comparison with a commercial PP mesh (each sample: 7 mm length \times 7 mm width). The meshes were elongated at 10% strain in each of L and T directions at 37 °C, followed by maintaining the elongation for 1800 s to determine the force for stress relaxation behavior. The force results were normalized following Equation (18), and the force reduction (%) and relaxation ratio were calculated using Equations (19) and (20), respectively:

$$\text{Normalized force} = \frac{\text{Force}}{F_{\text{initial}}} \quad (18)$$

$$\text{Force reduction} = \frac{[F_{\text{initial}} - F_{\text{end}}]}{F_{\text{initial}}} \times 100 \quad (19)$$

$$\text{Relaxation ratio} = \frac{F_{\text{initial}}}{F_{\text{end}}} \quad (20)$$

In Equations (18–20), F_{initial} is the initial force, and F_{end} is the force after 1800 s ($N = 3$, each group).

Moldable Property of BMR Mesh: As a model of abdomen, a hemisphere structure (3 mm diameter \times 1.5 mm height) was 3D printed (Raised3D Pro2, Irvine) using polylactic acid (PLA). BMR mesh samples were heated for 120 s at each of 36 °C, 43 °C, and 51 °C, followed by placing on the hemisphere by pressing for 1 min. After releasing the pressure force, the deformation degree of each sample was determined to examine the moldable property. The duration of heat energy accumulation to mold was determined using PCL/PCL-PGMA films (3 mm width \times 30 mm length, 0.3 mm thickness). The films were heated at 43 °C for 30 and 120 s, respectively, followed by twist-wrapping onto a glass rod with pressing for 1 min so that the molding completeness to a twist-wrap was examined below T_m .

FEA for Motion Reactor Design: To culture HDFs under abdomen-like cyclic mechanical stress in vitro, a model of motion reactor, with three layers: silicone membrane, mesh sample, and gluing gelatin gel, was designed using the Fusion 360 CAD program (version 2018, Autodesk, California, USA). The directional mechanical data of test mesh groups (ADM, PP, and BMR) were obtained by tensile analysis and entered it into ANSYS

workbench software. The hyper-elastic character of acellular dermal matrix (ADM) required curve fitting with mooney-rivlin 2 parameter model using ANSYS, thereby setting C10 and C01 to 0.05 MPa and 0.274 MPa, respectively. The Young's modulus of PP was set to 20 MPa as an isotropic linear elastic material.^[46] The storage modulus of the cross-linked gelatin hydrogel was set to 2000 kPa as reported previously.^[47] The thickness of the hydrogel and mesh was set to 1 mm in contrast to 0.1 mm of silicone membrane. Subsequently, the air pressure (120 mm Hg) was applied to inflate the bottom membrane, thereby determining the strain and stress to deform the gel where HDFs were embedded through an iterative calculation using ANSYS MPDL module.

Motion Reactor System: As determined by FEA, the motion reactor was developed by first 3D printing (Raised3D Pro2) of cuboid PLA structure (2 cm length × 2 cm width × 0.5 cm height) with molding into PDMS to construct the air (bottom) and media (top) chambers. A silicone sheet (0.1 mm thickness, HSW, Gyeonggi-do, Republic of Korea) was attached to the PDMS mold through surface modification in-between the air and media chambers so that the two chambers were separated. As the cyclic motion of membrane layers should be synchronized upon changes in the air pressure, dopamine was treated to the silicone surface to bond with test mesh samples. Hence, dopamine hydrochloride (2 mg, H8502, Sigma-Aldrich) was dissolved in 10 mm Tris-HCl, pH 8.5 (1 mL, BT021A, Biosolution, Gyeonggi-do, Republic of Korea), which was sprayed on the silicone sheet, followed by overnight incubation at room temperature. The silicone surface was washed to remove the dopamine solution and dried for 12 hours. Mesh samples were placed onto the silicone sheet by gluing and gelation of gelatin hydrogel (5% w/v, G1890, Sigma-Aldrich) upon cross-linking reaction with m-transglutaminase (mTG, 1% w/v, Modernist Pantry, Eliot, ME, USA) at 37 °C for 30 min.

Fibroblast Response to the Reactor Motion: HDF was purchased from American Type Culture Collection (ATCC; Manassas, VA, USA) and cultured using the Dulbecco's modified Eagle's medium-low glucose (DMEM; Gibco, Massachusetts, USA) with supplementation of fetal bovine serum (FBS; 10% v/v, Gibco) and penicillin-streptomycin (PS; 1% v/v, Gibco). HDFs (2×10^4 cells cm^{-2}) were seeded onto the gelatin hydrogel of motion reactor for 24 h in an incubator (37 °C, 5% CO_2). The motion reactor was connected to syringe pump (LEGATO210, KdScientific, Holliston, MA, USA) using straight connectors (30622-49, Donginbio, Seoul, Republic of Korea) and silicone tube (I.D. = 1 mm, O.D. = 2 mm; SL-0102, LK LAB Korea, Gyeonggi-do, Republic of Korea; Figure S8, Supporting Information).

The inflation pressure of the air chamber was set at 120 mm Hg in alignment with the peak pressure of the abdominal wall during exercising or coughing,^[48] thereby operating the cyclic pressure circumstance (every 2-h peak pressure). HDFs were cultured on the reactor for 1, 3, and 7 days, and cell viability was determined using Live/DEAD Viability/Cytotoxicity Kit (L3324, Invitrogen, Waltham, MA, USA) following the manufacturer's protocol. Briefly, cells were incubated with 4 mM calcein-AM (live-green) and 2 mM ethidium homodimer-1 (dead-red) for 30 min in the culture media with counterstaining of nuclei with NucBlue (Invitrogen), followed by confocal imaging (LSM 980; Zeiss, Oberkochen, Land Baden-Württemberg, Germany) with quantitative analysis using ImageJ (N = 4, each group).

Rat Hernioplasty: SD rats (female, 12 weeks old, Orient Bio, Seoul, Republic of Korea) were anesthetized through intramuscular injection of tiletamine-zolazepam (50 mg kg^{-1} , Zoletil, Virbac Korea) and xylazine (10 mg kg^{-1} , Rompun, Bayer Korea) into the right thigh, and isoflurane (<2.5%, Piramal, PA, USA) inhalation was maintained during surgical procedure. After placing the rat in the supine position, the lower abdomen area was shaved and sterilized it with povidone-iodine (Green Pharmaceutical, Jincheon, Republic of Korea). Partial thickness defects (0.5 cm × 0.5 cm/each) were made by incision into the left and right sides of anterior-lower abdominal at 1 cm from the midline.^[49] The defects were made into the layers of skin, subcutaneous fat, fascia, and external oblique muscle layer of the abdominal wall by preserving the parietal peritoneum, internal oblique muscle, and transversus abdominis muscle with prevention of any damage to the superficial epigastric artery.

Then, sample meshes were placed to cover the defect center in-between the parietal peritoneum and subcutaneous tissue. The honeycomb and BMR meshes underwent shape molding to fit into the abdominal wall anatomy by injecting sterilized 43 °C saline for 120 s. The defects with sample implantation were sutured with 5-0 ethilon (W1661G, Ethicon, New Jersey, USA), and no implantation with only suturing 4-0 vicryl (W9113, Ethicon) served as a surgical control. The rats were carefully monitored daily for 2 weeks until sacrifice (N = 5, each group). The structural stability of hernia mesh was determined by obtaining the gross photo images with image J processing on day 0 (before) and 14 after mesh deployment for the abdominal hernioplasty upon euthanizing rats. The Image J software was used to extract the pattern details of mesh structure, and the consistency rate was calculated through angle analysis from the pattern details.

Immunostaining and Histology: The hydrogel of motion reactor was rinsed with PBS (Welgene, Gyeongsangbuk-do, Republic of Korea). HDFs were fixed with 4% paraformaldehyde (CellNest, Gyeonggi-do, Republic of Korea) for 1 h; they were permeabilized with 0.1% Triton X-100 (Sigma-Aldrich) in PBS and then blocked with 5% bovine serum albumin (BSA; Millipore, Burlington, MA, USA) at room temperature for 1 h (N = 4, each group).

Next, primary antibodies were added to each sample for staining of Ki67 (1:250, ab16667, Abcam, Cambridge, UK), α -SMA (1:200, ab7817, Abcam), collagen type 1 (1:200, PA5-29569, Invitrogen) and collagen type 3 (1:200, ab6310, Abcam) overnight at 4 °C, followed three washes with PBS. Secondary antibodies (1:1000, Alexa Fluor 488, and Alexa Fluor 594, Jackson ImmunoResearch Laboratories, West Grove, PA, USA) were added to each sample for 2 h at room temperature in the dark. The cytoskeleton was stained by treating phalloidin (Invitrogen) with counterstaining of nuclei with NucBlue (Invitrogen). All samples were subjected to confocal imaging (LSM 980).

Rat tissues with mesh samples were harvested, rinsed with PBS, and fixed in 10% paraformaldehyde (Biosesang) for 24 h. The samples were embedded in paraffin wax, sectioned into 5 μm slice, and followed by deparaffinization and rehydration with xylene (Duksan, Gyeonggi-do, Republic of Korea) and ethyl alcohol (Duksan) for staining analyses (N = 5, each group). The samples were first subjected to H&E staining with optical imaging, and the vessel number was counted in the high-power field (HPF; 400 \times) images. Masson trichrome staining was carried out with optical imaging, and the images were processed through Orientation J plugin of Image J software (National Institute of Health) to determine the origin of collagen fiber.

Sirius red staining was carried out (ab150681, Abcam) following the manufacturer's instruction by incubating the samples in Picro sirius red solution for 1 h, followed by rinsing with acetic acid solution, washing with PBS, and dehydrating with alcohol. Then, the images were taken by light microscopy with polarized films (KENIS, Kita-ku, Osaka, Japan). For immunofluorescence staining, antigen retrieval was conducted with citrate buffer (1X, pH 6.0, Sigma-Aldrich) by heating for 30 min at 95 °C, followed by blocking with 0.1% Triton X-100 (Sigma-Aldrich) and 5% bovine serum albumin (BSA) in PBS for 2 h at room temperature. The samples were then incubated with primary antibodies of the collagen type 1 (1:100, NB600-450, Novus, St. Charles, MO, USA), collagen type 3 (1:100, NB600-594, Novus), α -SMA (1:200, ab5694, Abcam), vimentin (1:200, NBP-44832, Novus), and CD31 (1:200, ab24590, Abcam) overnight at 4 °C. Then, the slides were washed with PBS and treated with secondary antibodies (1:1000, Alexa Fluor 488 and Alexa Fluor 594, Jackson ImmunoResearch Laboratories) for 2 h at room temperature. Nuclei were counterstained with DAPI (H1200, Vectashield, Darmstadt, Germany), followed by confocal imaging (LSM 980) with quantitative analysis using image J (NIH).

Gene Expression: Total RNA was extracted from cells and tissues by treating with TRIzol reagent (15596026, Life Technologies, Carlsbad, CA, USA) using an RNA extraction kit (74106, Qiagen, Hilden, Germany), according to the manufacturer's protocol, followed by determining the RNA concentration in a Nanodrop 2000 Spectrophotometer (ND 2000, Thermo Fischer). Complementary DNA (cDNA) was synthesized using AccuPower CycleScript RT Premix (K2044, Bioneer, Daejeon, Republic of Korea) and

PCR Thermal Cycler (T100, Bio-Rad Laboratories, Hercules, CA, USA). qRT-PCR (StepOne V2.3, Applied Biosystems, MA, USA) was conducted with cDNA, SYBER Green PCR mix (Applied Biosystems), and primers (Table S2, Supporting Information). Gene expression was normalized to glyceraldehyde 3-phosphate dehydrogenase (GAPDH) and analyzed using the $2^{-\Delta\Delta Ct}$ method.

Statistical Analysis: All experimental data were presented as mean \pm standard deviation (SD) with at least three replicates, and statistical analyses were conducted using Sigmaplot (V12.0, Systat Software, CA, USA). The statistical significance was analyzed using a one-way analysis of variance (ANOVA) with Bonferroni's and Tukey's post-hoc analysis and an unpaired Student's *t*-test. Values of $*p < 0.05$, $**p < 0.01$, and $***p < 0.001$ were considered statistically significant (NS: non-significant).

Supporting Information

Supporting Information is available from the Wiley Online Library or from the author.

Acknowledgements

H.H., C.H.L., and K.S.L. contributed equally to this work. The Korea Medical Device Development Fund Grant funded by the Ministry of Science and ICT, Ministry of Trade, Industry and Energy, Ministry of Health & Welfare, and Ministry of Food and Drug Safety (RS-2020-KD000152) and the National Research Foundation (NRF) of Korea Grant funded by the Korean Government (MSIP) (NRF-RS-2023-00207857) financially supported this study. The MD-PhD/Medical Scientist Training Program through the Korea Health Industry Development Institute (KHIDI), funded by the Ministry of Health and Welfare, also supported this work.

Conflict of Interest

The authors declare no conflict of interest.

Data Availability Statement

The data that support the findings of this study are available from the corresponding author upon reasonable request.

Keywords

abdominal motion, computational simulations, hernia mesh, metamaterials, rat hernioplasty, shape configuration

Received: April 19, 2023

Revised: June 27, 2023

Published online:

- [1] L.-M. Zhu, P. Schuster, U. Klinge, *World J. Gastrointestinal Surg.* **2015**, *7*, 226.
- [2] X. Yu, J. Zhou, H. Liang, Z. Jiang, L. Wu, *Prog. Mater. Sci.* **2018**, *94*, 114.
- [3] Y. Li, W. Li, T. Han, X. Zheng, J. Li, B. Li, S. Fan, C.-W. Qiu, *Nat. Rev. Mater.* **2021**, *6*, 488.
- [4] T. Brunet, A. Merlin, B. Mascaro, K. Zimny, J. Leng, O. Poncelet, C. Aristégui, O. Mondain-Monval, *Nat. Mater.* **2015**, *14*, 384.
- [5] R. Grimberg, *Mater. Sci. Eng., B* **2013**, *178*, 1285.
- [6] B. Pérez-Köhler, S. Benito-Martínez, V. Gómez-Gil, M. Rodríguez, G. Pascual, J. M. Bellón, *Materials* **2021**, *14*, 7092.
- [7] T. Saha, X. Wang, R. Padhye, S. Houshyar, *OpenNano* **2022**, 100046.
- [8] D. L. Sanders, A. N. Kingsnorth, *Expert Rev. Med. Devices* **2012**, *9*, 159.
- [9] A. L. Nolfi, B. N. Brown, R. Liang, S. L. Palcsey, M. J. Bonidie, S. D. Abramowitch, P. A. Moalli, *Am. J. Obstet. Gynecol.* **2016**, *215*, 206.e1.
- [10] C. W. See, T. Kim, D. Zhu, *Engineered Regeneration* **2020**, *1*, 19.
- [11] B. Klosterhalfen, U. Klinge, *J. Biomed. Mater. Res., Part B* **2013**, *101*, 1393.
- [12] Z. Liu, N. Wei, R. Tang, *ACS Biomater. Sci. Eng.* **2021**, *7*, 2064.
- [13] B. Hernández-Gascón, A. Mena, E. Peña, G. Pascual, J. Bellón, B. Calvo, *Ann. Biomed. Eng.* **2013**, *41*, 433.
- [14] J. C. Maxwell, *J. Sci.* **1864**, *27*, 294.
- [15] J. Y. Park, J. B. Lee, W. B. Shin, M.-L. Kang, Y. C. Shin, D. H. Son, S. W. Yi, J.-K. Yoon, J. Y. Kim, J. Ko, *Acta Biomater.* **2020**, *101*, 273.
- [16] N. Qamar, N. Abbas, M. Irfan, A. Hussain, M. S. Arshad, S. Latif, F. Mehmood, M. U. Ghorri, *J. Drug Deliv Sci Technol* **2019**, *53*, 101164.
- [17] B. Hinz, *J. Biomech.* **2010**, *43*, 146.
- [18] R. A. Clark, K. Ghosh, M. G. Tonnesen, *J. Invest. Dermatol.* **2007**, *127*, 1018.
- [19] F. G. Thankam, G. Palanikumar, R. J. Fitzgibbons, D. K. Agrawal, *J. Surg. Res.* **2019**, *236*, 134.
- [20] K. Junge, U. Klinge, R. Rosch, P. R. Mertens, J. Kirch, B. Klosterhalfen, P. Lynen, V. Schumpelick, *Langenbecks Arch Surg* **2004**, *389*, 17.
- [21] N. Henriksen, D. Yadete, L. Sorensen, M. Ågren, L. Jorgensen, *Journal of British Surgery* **2011**, *98*, 210.
- [22] S. Koruth, Y. N. Chetty, *Annals of medicine and surgery* **2017**, *19*, 37.
- [23] Y. C. Shin, J. B. Lee, D. H. Kim, T. Kim, G. Alexander, Y. M. Shin, J. Y. Park, S. Baek, J. K. Yoon, Y. J. Lee, *Adv. Mater.* **2019**, *31*, 1904476.
- [24] W. T. Oh, J. B. Lee, W. Choi, H. W. Bae, C. S. Kim, C. Y. Kim, H.-J. Sung, *ACS Biomater. Sci. Eng.* **2020**, *6*, 3784.
- [25] H.-S. Kim, J. Park, H.-S. Ha, S. Baek, C. H. Lee, K. Lee, S. Park, J. Kim, S. W. Yi, H.-J. Sung, *Research* **2023**, *6*, 0137.
- [26] E. Dogan, A. Bhusal, B. Cecen, A. K. Miri, *Appl. Mater. Today* **2020**, *20*, 100752.
- [27] C. Yang, M. Boorugu, A. Dopp, J. Ren, R. Martin, D. Han, W. Choi, H. Lee, *Mater. Horiz.* **2019**, *6*, 1244.
- [28] V. Deshpande, M. Ashby, N. Fleck, *Acta Mater.* **2001**, *49*, 1035.
- [29] V. Tawde, S. Chaurasia, S. Gupta, R. Rastogi, A. K. Dantuluri, W. Liu, S. McMahon, D.-W. Seo, *Yakhak Hoechi* **2022**, *66*, 1.
- [30] W. Zhao, L. Liu, F. Zhang, J. Leng, Y. Liu, *Mater. Sci. Eng., C* **2019**, *97*, 864.
- [31] N. Sanbhal, L. Miao, R. Xu, A. Khatri, L. Wang, *J. Ind Text* **2018**, *48*, 333.
- [32] M. Avrami, *J. Chem. Phys.* **1939**, *7*, 1103.
- [33] R. De Juana, A. Jauregui, E. Calahorra, M. Cortazar, *Polymer* **1996**, *37*, 3339.
- [34] G. Xu, L. Du, H. Wang, R. Xia, X. Meng, Q. Zhu, *Polym. Int.* **2008**, *57*, 1052.
- [35] H. E. Kissinger, *Anal. Chem.* **1957**, *29*, 1702.
- [36] T. Ozawa, *Bull. Chem. Soc. Jpn.* **1965**, *38*, 1881.
- [37] P. C. Liacouras, D. Sahajwalla, M. D. Beachler, T. Sleeman, V. B. Ho, J. P. Lichtenberger, *3D Print Med* **2017**, *3*, 1.
- [38] Y. J. Choi, T. G. Kim, J. Jeong, H. G. Yi, J. W. Park, W. Hwang, D. W. Cho, *Adv. Healthcare Mater.* **2016**, *5*, 2636.
- [39] Q. Zhao, J. Wang, H. Cui, H. Chen, Y. Wang, X. Du, *Adv. Funct. Mater.* **2018**, *28*, 1801027.
- [40] Q. Zhao, J. Wang, Y. Wang, H. Cui, X. Du, *Natl Sci Rev* **2020**, *7*, 629.
- [41] M. Peng, Q. Zhao, M. Wang, X. Du, *Nanoscale* **2023**, *15*, 6105.

- [42] L. J. Gibson, *MRS Bull.* **2003**, 28, 270.
- [43] F. Ongaro, *Theor. Appl. Mech. Lett.* **2018**, 8, 209.
- [44] H. E. Kissinger, *J. Res. Natl. Bur. Stand.* **1956**, 57, 217.
- [45] J. H. Flynn, L. A. Wall, *J Polym Sci B* **1966**, 4, 323.
- [46] J. L. Van Eps, A. Chaudhry, J. S. Fernandez-Moure, C. Boada, V. Chegireddy, F. J. Cabrera, S. Tang, E. Tasciotti, R. Righetti, *Surgical endoscopy* **2019**, 33, 2802.
- [47] M.-L. Kang, H.-S. Kim, J. You, Y. S. Choi, B.-J. Kwon, C. H. Park, W. Baek, M. S. Kim, Y. J. Lee, G.-I. Im, *Sci. Adv.* **2020**, 6, eaay-5413.
- [48] W. S. Cobb, J. M. Burns, K. W. Kercher, B. D. Matthews, H. J. Norton, B. T. Heniford, *J. Surg. Res.* **2005**, 129, 231.
- [49] B. Pérez-Köhler, S. Benito-Martínez, M. Rodríguez, F. García-Moreno, G. Pascual, J. Bellón, *Hernia* **2019**, 23, 789.